

Finite-temperature elasticity phase transition in decagonal quasicrystals

Hyeong-Chai Jeong and Paul J. Steinhardt

Department of Physics, University of Pennsylvania, Philadelphia, Pennsylvania 19104

(Received 12 April 1993)

We present evidence for a finite-temperature phase transition in the phason elasticity of quasicrystals. A tiling model for energetically stabilized decagonal quasicrystals has been studied in an extensive series of Monte Carlo simulations. The Hamiltonian (energetics) of the model is given by nearest-neighbor Penrose-like matching rules between three-dimensional unit cells. A new order parameter and diagnostics have been introduced. We show that a transition from locked-phason to unlocked-phason dynamics occurs at finite temperature. In the unlocked phase, phasons can be thermodynamically excited even though the quasicrystal is energetically stabilized at low temperatures.

I. INTRODUCTION

Quasicrystals exhibit two distinct types of low-energy elastic (hydrodynamic) excitations—phonons and phasons.¹ In this paper we consider the temperature-dependent behavior of the phason elasticity in three-dimensional quasicrystals with decagonal symmetry: a solid that can be described as a stack of periodically spaced planes, which each exhibit tenfold symmetry.² We present evidence for a finite-temperature phase transition in the phason elasticity, apparently analogous to the pinning transition found in the one-dimensional Frenkel-Kontorova (FK) model.³

Quasicrystals are new types of solids, which have a discrete point-group symmetry that is forbidden for crystals such as fivefold symmetry in two-dimensions and icosahedral symmetry in three dimensions.⁴ These quasicrystals possess a long-range translational order known as quasiperiodicity. The recent experiments on AlCoCu showed the existence of thermodynamically stable decagonal quasicrystals.⁵ What makes the quasicrystals stable? Two possibilities that have been debated are energetic stability and entropic stability.⁶ In the energetically stabilized quasicrystal model, microscopic interaction energy has its minimum when atoms are arranged in a quasiperiodic structure. Such interactions ensure that the low-temperature equilibrium state is quasicrystalline. In the entropically stabilized quasicrystal model, the entropy that arises from thermodynamically excited atomic relocations (specifically, phasons) makes the quasicrystal stable. In this model, quasicrystals are not stable at low temperature.

In this paper, we consider the phason dynamics of an energetically stabilized tiling model for the decagonal phase. The interactions are prescribed so that quasicrystals remain stable as the temperature T approaches zero. A tile is an idealization of presenting a cluster of atoms in a real material. The energetics are mimicked by nearest-neighbor matching rules, which are generalizations of the Penrose edge-matching rules for two-dimensional tilings. We assign a finite energy to each mismatch in a given

configuration. This guarantees that the state of lowest energy is a perfect quasicrystal. This is to be contrasted with a random tiling model, used to represent the limiting case of entropically stabilized quasicrystals, in which the same energy is assigned to every configuration and a quasicrystal symmetry is favored due to the high entropy.

Phonons and phasons are low-energy hydrodynamic modes associated with quasiperiodic broken translational symmetry. At long wavelengths, phonons correspond to uniform translations, and phasons correspond to rearrangements of atoms from one perfect quasicrystal lattice to another. In a tiling picture of quasicrystals, the phason degrees of freedom correspond to the rearrangements of tiles. Finite-wavelength phasons produce rearrangements, which violate the matching rules and hence cost finite energy. If $\mathbf{w}(x)$ is the phason field, then fixed phason strains produce a number of mismatches proportional to $|\Delta\mathbf{w}|$. Consequently, the elastic energy is $F \sim |\Delta\mathbf{w}|$, a nonanalytic form. We shall call a finite-temperature state in which the elastic energy has this form a “locked phase,”⁷ since the phasons cannot be thermodynamically excited (no phason Debye-Waller contribution). An alternative type of quasicrystal is described by the continuum density wave picture in which the elastic free energy grows $F \sim (\Delta\mathbf{w})^2$. This density wave picture corresponds to a distinct elastic phase, which we shall refer to as the “unlocked phase.” In this phase, phasons have thermal excitations analogous to phonons. Historically, the locked phase has been assumed to be characteristic of any energetically stabilized quasicrystal, whereas entropically stabilized quasicrystals are, by definition, in the unlocked phase with square-gradient elasticity. Our point here is to show that this view is not correct in general. Rather it is possible in energetically stabilized quasicrystals to have a novel elastic phase transition from a locked phase at low temperature to unlocked phase at high temperature as had been speculated by Socolar *et al.*⁸ We note that this behavior is different from two-dimensional (2D) behavior, where both energetic and entropic models have unlocked elasticity at any finite temperature.^{9,10} Hence, the observation of unlocked elastic behavior (the

phason Debye-Waller effect) at finite temperature is not a proof of entropic stability.

The organization of the paper is as follows. In Sec. II, we define our model for studying decagonal phase quasicrystals. In Sec. III, we present the characteristics of the system we use for Monte Carlo simulation. The algorithms of Monte Carlo runs are also presented. Section IV presents diagnostics for studying the phase transition in phason elasticity. We introduce the notion of “lane width” and “trail magnetization” to check if the system is in the locked phase. The results of the Monte Carlo simulation are presented here. Section V, the Conclusion, summarizes our results and discusses the potential connection to the experiment.

II. DEFINING MODELS

Our model for 3D quasicrystals with decagonal symmetry has two types of unit cells: skinny and fat. Each cell is the shape of a prism with a rhombic cross section whose upper and lower faces are the shape of Penrose rhombuses. In the zero-temperature ground state, each layer viewed along the tenfold axis resembles a perfect Penrose tiling. The 2D Penrose edge rules are replaced by “side face” rules, referring to tile faces that join tiles in the same layer. Side faces of the unit cells have single or double arrow marks as shown in Fig. 1 so that the tiling consistent with matching rules—joining side face to side face according to the same arrow marks, is the perfect quasiperiodic Penrose tiling.

We assign mismatch energy ϵ_1 for a violation of single arrow marks. Double arrow mismatches are not allowed (mismatch energy for a double arrow mismatch is

$$\epsilon_{\text{intralayer}} = \begin{cases} 0 & \text{for an arrow matched side face} \\ \epsilon_1 & \text{for a single arrow mismatched side face} \\ \infty & \text{for a double arrow mismatched side face,} \end{cases}$$

and

$$\epsilon_{\text{interlayer}} = \begin{cases} 0 & \text{for an upper (lower) face that coincides with lower (upper) face of an upper (lower) unit} \\ \epsilon_2 & \text{for an upper (lower) face which does not coincide with the lower (upper) face of an upper (lower) unit.} \end{cases}$$

Henceforth we will refer to intralayer mismatches as “arrow mismatches” and interlayer mismatches as “face mismatches.”

In the finite-temperature Monte Carlo (MC), we introduce “flips” of single hexagonal prisms within a layer. There are two kinds of hexagonal prisms, which we shall call D -type hexagonal prisms and Q -type hexagonal prisms, respectively. A D (Q)-type hexagonal prism consists of two fat cells and one skinny cell (one fat cell and two skinny cells), and its top view is a D (Q)-type hexagon.¹¹ Each hexagonal prism can be uniquely identified by the vertex at the center of the upper hexagon. Figure 2 shows hexagonal prism before and after flips. Solid circles indicate the center vertices of the upper hexagons.

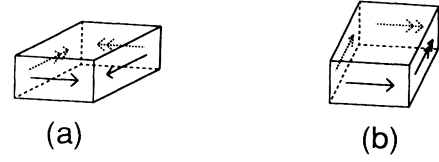


FIG. 1. (a) Skinny cell: Upper and lower faces are in the shape of a Penrose skinny rhombus. Side faces have arrow marks according to the arrow patterns of the Penrose skinny rhombus. (b) Fat cell: Upper and lower faces are in the shape of a Penrose fat rhombus. Side faces have arrow marks according to the arrow patterns of the Penrose fat rhombus.

infinity) in order to study purely phason dynamics [see discussion below Eq. (3)]. The 3D decagonal model is introduced by considering a stack of these layers. We fix the interlayer interaction energy to have its minimum when configurations of two layers are identical (fat tile directly on fat tile, skinny directly on top of skinny). We assign stacking direction face mismatch energy ϵ_2 when the vertices of an upper (lower) face of a unit cell do not coincide with those of a lower (upper) face of an upper (lower) unit cell. The energy of tiling is defined as the sum of the intralayer interaction energy (arrow mismatch energy) and interlayer interaction energy (stacking direction face mismatch energy):

$$E = E_{\text{intralayer}} + E_{\text{interlayer}} = \sum_{\text{side faces}} \epsilon_{\text{intralayer}} + \sum_{\text{upper, lower faces}} \epsilon_{\text{interlayer}}, \quad (1)$$

where

A hexagonal prism flip from a ground state makes two arrow mismatches and six face mismatches. Hence, the net energy cost is $2\epsilon_1 + 6\epsilon_2$.

For most of our MC runs, we impose a “stacking constraint”: For a given hexagonal prism, flipping is allowed only when there is a hexagonal prism in the adjacent upper (or lower) layer whose lower (upper) hexagon has a boundary that coincides (ignoring center vertex) with the boundary of upper (lower) hexagon of the given hexagonal prism. This constraint is necessary for “interlayer flips.”^{7,12}

Let us define phason variables in this model. The position of any vertex of the tiling with fixed origin (by choosing a vertex as the origin) is expressed as

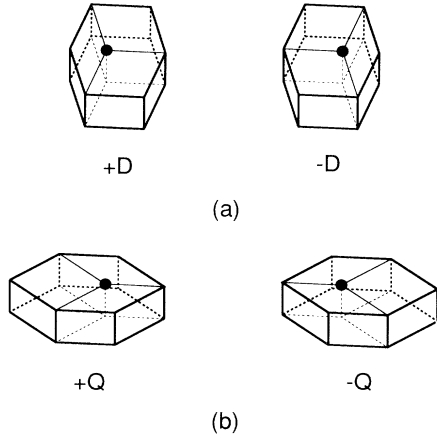


FIG. 2. Hexagonal prisms: (a) D -type hexagonal prism before ($+D$) and after ($-D$) flip. (b) Q -type hexagonal prism before ($+Q$) and after ($-Q$) flip. Solid circles indicate the center vertices of the upper hexagons. The orientation (\pm sign) is given by the convention explained in the text (Sec. IV C).

$$\mathbf{x} = \sum_{\alpha=0}^5 n_{\alpha} \mathbf{e}_{\alpha}^{\parallel}, \quad (2)$$

where $\mathbf{e}_{\alpha}^{\parallel} = (\cos \frac{2\pi\alpha}{5}, \sin \frac{2\pi\alpha}{5}, 0)$ for $\alpha = 0, 1, \dots, 4$ and $(0, 0, 1)$ for $\alpha = 5$ and n_{α} is the number of steps in direction $\mathbf{e}_{\alpha}^{\parallel}$ on a continuous path to the vertex at \mathbf{x} from the origin along the edges, counting negatively when going in the $-\mathbf{e}_{\alpha}^{\parallel}$. We define a complementary basis $\mathbf{e}_{\alpha}^{\perp}$, such that the vectors $\mathbf{e}_{\alpha} = \mathbf{e}_{\alpha}^{\perp} \oplus \mathbf{e}_{\alpha}^{\parallel}$ are linearly independent in 6D hyperspace. Then, for each vertex \mathbf{x} whose position is given by Eq. (2), we define a perp-space position vector \mathbf{x}^{\perp} by

$$\mathbf{x}^{\perp} = \sum_{\alpha=0}^5 n_{\alpha} \mathbf{e}_{\alpha}^{\perp}, \quad (3)$$

where $\mathbf{e}_{\alpha}^{\perp} = (\cos \frac{4\pi\alpha}{5}, \sin \frac{4\pi\alpha}{5}, 1)$ for $\alpha = 0, 1, \dots, 4$ and $(0, 0, 0)$ for $\alpha = 5$. These vectors span a 3D space called “perp-space,” which can be further decomposed as the product of a 2D “phason space” (which is incommensurately oriented with respect to the hyperspace lattice) and a 1D “discrete space” (which is commensurately oriented). In our model in which double arrow mismatches are disallowed, the discrete space component of \mathbf{x}^{\perp} is restricted to four consecutive integers. Phason variables \mathbf{w} are to be defined as a smoothed function $\mathbf{w}(\mathbf{x})$, constructed as an average of the phason space projection $\mathbf{x}_{\text{ph}}^{\perp}$ of the perp-space position vector \mathbf{x}^{\perp} , in some neighborhood of radius $a_0 \gg 1$.

III. MONTE CARLO SIMULATION

We use a thermal Monte Carlo methods based on a Metropolis importance sampling scheme.¹³ The basic Monte Carlo move is (1) randomly select a hexag-

onal prism and (2) if it satisfies the stacking direction constraint, flip it according to a probability; $p = \exp(-\beta\Delta E)$ if $\Delta E > 0$, $p = 1$ otherwise, where ΔE is the energy cost for performing the flip. We used an approximant to a 2D perfect Penrose tiling for a layer that has the smallest phason strain at a given system size with periodic boundary conditions. To get a periodic tiling, we use a periodic uniform dual grid, which is the intersection of 4D lattice planes of the 5D hypercubic lattice with a 2D hypersurface spanned by two vectors,

$$\boldsymbol{\omega}_1 = (P, 0, -P, -Q, Q), \quad \boldsymbol{\omega}_2 = (0, P, Q, -Q, -P), \quad (4)$$

where P and Q are integers. A sequence of approximants are obtained by taking $P = F_k$ and $Q = F_{k-1}$, where F_k is k th Fibonacci number ($F_0 = 0$, $F_1 = 1$). Then the basis vectors of the periodic tiling are given by

$$\mathbf{L}^{(1)} = \tau^k \left(\frac{2\tau - 1}{2}, -\frac{1}{\tau} \sin \frac{\pi}{5} \right), \quad (5)$$

$$\mathbf{L}^{(2)} = \tau^k \left(0, 2 \sin \frac{\pi}{5} \right),$$

and the uniform phason strain \mathbf{E} to get the k th periodic approximant is

$$\mathbf{E} = (-1)^{k+1} \tau^{-2k} \begin{pmatrix} 1 & 0 \\ 2 \sin \frac{2\pi}{5} & \tau \end{pmatrix}. \quad (6)$$

When we calculate perp-space position vectors, to get rid of the effects due to the uniform phason strain \mathbf{E} , we replace $\mathbf{e}_{\alpha}^{\perp}$ in Eq. (3) by $\mathbf{e}_{\alpha}^{\perp} - \mathbf{E} \mathbf{e}_{\alpha}^{\parallel}$. The number of tiles in a layer is given by $N_k = F_{2k+1} + 2F_{2k}$. Since our main interest is the properties of 3D objects, the number of layers L_z of the systems is proportional to the size of a layer ($L_z = F_k$ for the k th approximant). Systems of 228 ($N_k \times L_z = 76 \times 3$), 995 (199×5), 4168 (521×8), and 17 732 (1364×13) tiles are used. We also study the effect of varying L_z for fixed L^1 and L^2 . For most of the models presented here, we have assigned interaction energy strength $\epsilon_1 = 1$ and $\epsilon_2 = 1/3$ in Eq. (1), corresponding to equal interlayer and intralayer energy costs for flipping an isolated hexagon beginning from the ground state.

We start out with an ordered configuration, with the minimum matching rule violations necessary to construct the periodic approximants. Data are taken following a heating sequence. We studied the time evolution of the data to check whether the system has been equilibrated. To ensure statistical independence, we measured the temporal correlations, and most case measurements are separated more than correlation time.¹⁴ Some cooling runs have been performed from above T_c to below T_c to check the presence of hysteresis effect. The data so obtained agree with high accuracy with those from heating studies. As a test of the algorithm, we assigned $\epsilon_2 = 0$ without the stacking direction constraint and got the known 2D Penrose model¹⁰ results.

IV. DIAGNOSTICS FOR PHASON ELASTICITY TRANSITION AND RESULTS OF MONTE CARLO SIMULATION

In the unlocked phase, where the continuum density wave picture is applied, the general form of the phason elastic free energy (up to quadratic in $\partial\mathbf{w}$) is

$$F = \frac{1}{2} \int d^3x K_1 [(\partial_x w_1)^2 + (\partial_y w_1)^2 + (\partial_x w_2)^2 + (\partial_y w_2)^2] + K_2 [(\partial_z w_1)^2 + (\partial_z w_2)^2] + K_3 [\partial_x w_1 \partial_y w_2 - \partial_y w_1 \partial_x w_2] \quad (8)$$

where K_1 , K_2 , and K_3 are elastic constants in the unlocked phase. The integration of the last term in a layer can be dropped to a line integral along the boundary of the layer that vanishes in the absence of dislocations.

On the other hand, in a locked phase the phason elastic free energy is given by

$$F = \frac{1}{2} \int d^3x \tilde{K}_1 (|\nabla_{\perp} w_1| + |\nabla_{\perp} w_2|) + \tilde{K}_2 (|\partial_z w_1| + |\partial_z w_2|), \quad (9)$$

where \tilde{K}_1 and \tilde{K}_2 are elastic constants in the locked phase, and $\nabla_{\perp} = \mathbf{e}_x \partial_x + \mathbf{e}_y \partial_y$ is a two-dimensional derivative in the plane perpendicular to the stacking direction (z axis).

To see whether a system is in a locked phase or in an unlocked phase, we could, in principle, compare the free energies of the systems with different uniform phason strain \mathbf{E} . To do this we would need to know the energy and the entropy of the system with low uniform background phason strain \mathbf{E} , as functions of temperature. We attempted to estimate the entropy, using the “energy method,” “the variance method,” and “the histogram method,”^{15,16} but we could not estimate entropy accurately enough to distinguish the phason elasticity. Hence, we resorted to several other measures including phason fluctuations, lane widths, and trail magnetization (defined below).

A. Phason fluctuations

The phason elastic free energy in the unlocked phase (8) can be diagonalized by Fourier transforming of phason variable $\mathbf{w}(\mathbf{x})$,

$$\mathbf{w}(\mathbf{p}) = V^{-1/2} \int d^3x e^{-i\mathbf{p}\cdot\mathbf{x}} \mathbf{w}(\mathbf{x}), \quad (10)$$

where V is the volume of the system. Then free energy (8) becomes

$$F = \frac{1}{2} \sum_{|\mathbf{p}| < 2\pi/a_0} K_1 (p_x^2 + p_y^2) [w_1(\mathbf{p})^2 + w_2(\mathbf{p})^2] + K_2 p_z^2 [w_1(\mathbf{p})^2 + w_2(\mathbf{p})^2]. \quad (11)$$

$$F = \frac{1}{2} \int d^d x K_{ijkl} \partial_i w_j \partial_k w_l, \quad (7)$$

where w_j is the j th component of phason variable and K_{ijkl} is an elastic constant tensor. For our model, due to the decagonal symmetry, the free energy of Eq. (7) reduces to the form

[We ignore the third term in Eq. (8), which vanishes in any configuration in our simulation.] Since the free energy (11) is harmonic in $w_i(\mathbf{p})$ for $i = 1, 2$, it is straightforward to calculate $\langle |\mathbf{w}(\mathbf{p})|^2 \rangle$,

$$\begin{aligned} \langle |\mathbf{w}(\mathbf{p})|^2 \rangle &= \sum_{i=1,2} \langle |w_i(\mathbf{p})|^2 \rangle \\ &= \frac{2}{K_1 (p_x^2 + p_y^2) + K_2 p_z^2}, \end{aligned} \quad (12)$$

where the angular brackets denote an ensemble average. Elastic constants K_1 and K_2 are obtained by measuring $\langle |\mathbf{w}(\mathbf{p})|^2 \rangle$ for $\mathbf{p} = p_x \mathbf{e}_x + p_y \mathbf{e}_y$ and for $\mathbf{p} = p_z \mathbf{e}_z$. Let us define

$$\begin{aligned} K_1(\mathbf{p}) &\equiv \frac{2}{\langle |\mathbf{w}(p_x, p_y, 0)|^2 \rangle (p_x^2 + p_y^2)}, \\ K_2(\mathbf{p}) &\equiv \frac{2}{\langle |\mathbf{w}(0, 0, p_z)|^2 \rangle p_z^2}. \end{aligned} \quad (13)$$

If the system is in the unlocked phase, $K_1(\mathbf{p})$ and $K_2(\mathbf{p})$ should be constants, independent of $|\mathbf{p}|$ for $2\pi/L < |\mathbf{p}| < \Lambda$, where L is the system size and Λ is the short-wavelength cutoff, which depends on the coarse graining scheme [Λ is order of $2\pi/a$ for a smooth function $\mathbf{w}(x)$, where a is the size of a unit cell]. A proper coarse graining scheme is necessary to get elastic constants by measuring $\langle |\mathbf{w}(\mathbf{p})|^2 \rangle$ in our simulation. This is because the perp-space position \mathbf{x}^{\perp} [from which a smooth function $\mathbf{w}(x)$ is constructed] fluctuates strongly for near-neighbor vertices ($\Delta\mathbf{x}^{\perp}/\Delta\mathbf{x} \sim 1$ for $\Delta\mathbf{x} \sim 1$).

We construct the phason field $\mathbf{w}(\mathbf{x})$ from the perp-space position \mathbf{x}^{\perp} by

$$\mathbf{w}(\mathbf{x}) = \int d^3x' K(\mathbf{x} - \mathbf{x}') S^{\perp}(\mathbf{x}'), \quad (14)$$

where $K(\mathbf{x})$ is a smearing kernel satisfying $\int d^3x K(\mathbf{x}) = 1$ and $S^{\perp}(\mathbf{x})$ is the representative surface—piecewise linear interpolating function of $\mathbf{x}_{\text{ph}}^{\perp}$. Precisely, we use

$$S^\perp(\mathbf{x}) = \begin{cases} \mathbf{x}_{\text{ph}}^\perp(\mathbf{x}) & \text{for } \mathbf{x} \text{ at a vertex of the upper face of a cell,} \\ \mathbf{x}_{\text{ph}}^\perp(\mathbf{x}_a)d_b + \mathbf{x}_{\text{ph}}^\perp(\mathbf{x}_b)d_a & \text{for } \mathbf{x} \text{ in an edge } (d_a \text{ from one end } \mathbf{x}_a, d_b \text{ from the other end } \mathbf{x}_b) \\ & \text{of the upper face,} \\ \frac{1}{2}[S^\perp(\mathbf{x}_1) + S^\perp(\mathbf{x}_2)] & \text{for } \mathbf{x} \text{ inside the upper face, where } \mathbf{x}_1 \text{ and } \mathbf{x}_2 \text{ are the projections} \\ & \text{of } \mathbf{x} \text{ to the edges (meet at a vertex) of the upper face,} \\ S^\perp(\mathbf{x}_{\text{up}}) & \text{for } \mathbf{x} \text{ inside the unit cell, where } \mathbf{x}_{\text{up}} \text{ is the projection of } \mathbf{x} \text{ to the upper face} \end{cases}$$

and

$$K(\mathbf{x}) = \frac{1}{4\pi} \frac{1}{r_{xy}} \Theta(2 - r_{xy}) \delta(z), \quad (15)$$

where $r_{xy} = (x^2 + y^2)^{1/2}$ and $\Theta(x)$ is the step function. When this coarse graining scheme is applied to the 2D Penrose model, the known elastic constants¹⁰ are recovered for $|\mathbf{p}| < \Lambda \simeq 1.5$. Note that a simple-minded coarse graining scheme to replace Eq. (15), $\mathbf{w}(\mathbf{x}) = \frac{V}{N} \sum_{i=1}^N \mathbf{x}_{\text{ph}}^\perp(\mathbf{x}_i) \delta(\mathbf{x} - \mathbf{x}_i)$ [$\mathbf{w}(\mathbf{p}) = \frac{V^{1/2}}{N} \sum_i \mathbf{x}_{\text{ph}}^\perp(\mathbf{x}_i) e^{-i\mathbf{p}\cdot\mathbf{x}}$] would not have worked as well. In the 2D Penrose model, the known elastic constants¹⁰ are recovered for only $|\mathbf{p}| < \Lambda \simeq 0.5$, which is nearly the long-wavelength cutoff ($2\pi/L$) for the systems in our simulation.

To determine if the system is in the unlocked phase, we measure whether $K_1(\mathbf{p})$ and $K_2(\mathbf{p})$ as defined in Eq. (13) are $|\mathbf{p}|$ independent. In Fig. 3, we show a plot of $K_1(\mathbf{p})$ and $K_2(\mathbf{p})$ vs $|\mathbf{p}|$ at $T = 1.5$ and 2.5 for a sequence of lattices of increasing size. These plots show that $K_1(\mathbf{p})$ and $K_2(\mathbf{p})$ are constants and independent of system size, indicating that the system is unlocked at $T > 1.5$. We estimate the elastic constants to be $K_1 = 1.72 \pm 0.02$, $K_2 = 0.56 \pm 0.02$ at $T = 1.5$ and $K_1 = 1.22 \pm 0.02$, $K_2 = 0.14 \pm 0.01$ at $T = 2.5$.

In contrast, Fig. 4 illustrates the same calculation for $T = 1.0$. Here, $K_1(\mathbf{p})$ and $K_2(\mathbf{p})$ fluctuate wildly with $|\mathbf{p}|$ and the mean value appears to diverge with increasing system size. Hence, $T = 1.0$ is clearly below a phase

transition (out of the unlocked phase). The wild behavior of $K_1(\mathbf{p})$ and $K_2(\mathbf{p})$ is consistent with the notion that the phason elastic energy is locked. Hence, phason fluctuation measurements can be used to establish a transition out of the unlocked phase described by an elastic energy of the form in Eq. (8). However, we cannot prove from phason fluctuation measurements that the low-temperature phase has $F \sim |\nabla \mathbf{w}|$ (as expected for a Penrose-tiling phase). This is because the phason fluctuations appear to become pinned (as indicated by the divergence of K_1 and K_2). Since \mathbf{w} is not thermodynamically excited, the dependence of F on $|\nabla \mathbf{w}|$ cannot be measured.

Further evidences of the transition from the unlocked phase is provided by the measurement of the average phason field within a layer,

$$\bar{\mathbf{w}}(z) = \frac{1}{S} \int_S \mathbf{w}(x, y, z) dx dy \quad (16)$$

(where S is the area of a layer), and then calculating how this average fluctuates from layer to layer. The average phason field within a layer $\bar{\mathbf{w}}(z)$ is related to the Fourier components of phason field at $p_x = p_y = 0$ by

$$\bar{\mathbf{w}}(z) = V^{-\frac{1}{2}} \sum_{p_z} \mathbf{w}(p_x = p_y = 0, p_z) e^{ip_z z}, \quad (17)$$

since

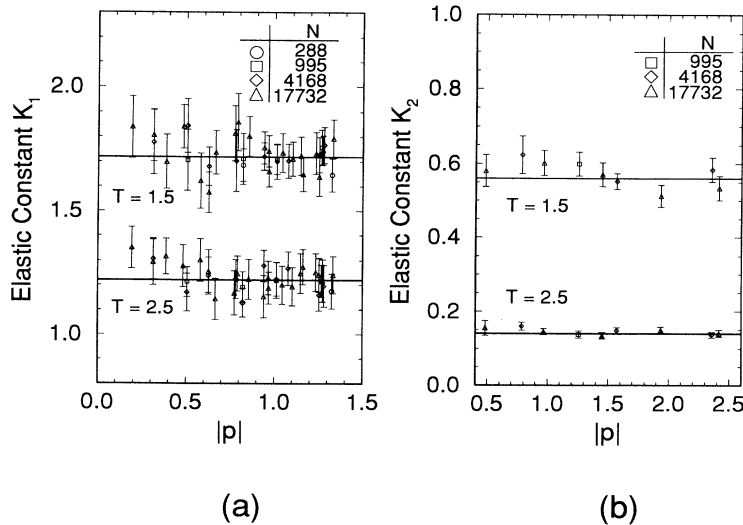


FIG. 3. The elastic constants $K_1(\mathbf{p})$ (a) and $K_2(\mathbf{p})$ (b) defined by Eq. (13) vs the magnitude of the wave vector $|\mathbf{p}|$ with unlocked phases (at $T = 1.5$ and $T = 2.5$). $K_1(\mathbf{p})$ and $K_2(\mathbf{p})$ are constant over $|\mathbf{p}|$ and independent of the system size. In this and the following figures, the numbers in the legend represent the numbers of tiles N in the systems.

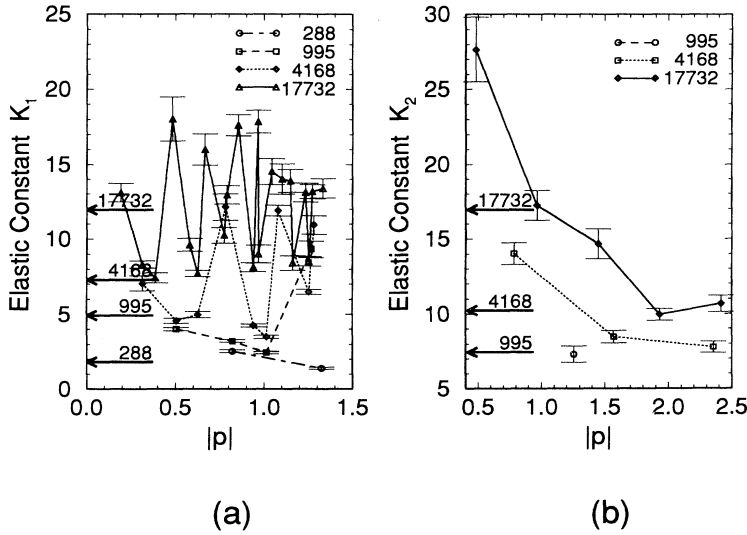


FIG. 4. The elastic constants $K_1(\mathbf{p})$ (a) and $K_2(\mathbf{p})$ (b) vs the magnitude of the wave vector $|\mathbf{p}|$ with locked phase (at $T = 1.0$). $K_1(\mathbf{p})$ and $K_2(\mathbf{p})$ increase in magnitude with increasing system size. Points of data for each system size are connected by lines shown in the legend. The average of K_i over $|\mathbf{p}|$ for each system size is indicated by an arrow.

$$\begin{aligned} \mathbf{w}(p_x = p_y = 0, p_z) &= V^{-\frac{1}{2}} \int \mathbf{w}(x, y, z) e^{-ip_z z} dz \\ &= \left(\frac{S}{L_z}\right)^{\frac{1}{2}} \int \bar{\mathbf{w}}(z) e^{-ip_z z} dz, \end{aligned} \quad (18)$$

where L_z is the number of layers. In an unlocked phase $|\mathbf{w}(p_x = p_y = 0, p_z)|^2 = 2/(K_2 p_z^2)$ [Eq. (12)]. Hence, the mean-square fluctuation of $\bar{\mathbf{w}}(z)$ in the unlocked phase,

$$\begin{aligned} \langle (\Delta \bar{\mathbf{w}})^2 \rangle &\equiv \frac{1}{L_z} \left\langle \left| \sum_z \bar{\mathbf{w}}(z) - \frac{1}{L_z} \sum_z \bar{\mathbf{w}}(z) \right|^2 \right\rangle \\ &= \frac{1}{V} \frac{L_z}{2\pi} \int_{c/L_z}^{c/a} \frac{2}{K_2 p_z^2} dp_z \\ &= \frac{2}{2\pi S c K_2} (L_z - a), \end{aligned} \quad (19)$$

where c is order of 2π and c/a is upper wave number cutoff. Figure 5 shows $\langle (\Delta \bar{\mathbf{w}})^2 \rangle$ vs L_z at $T = 1, 1.5,$

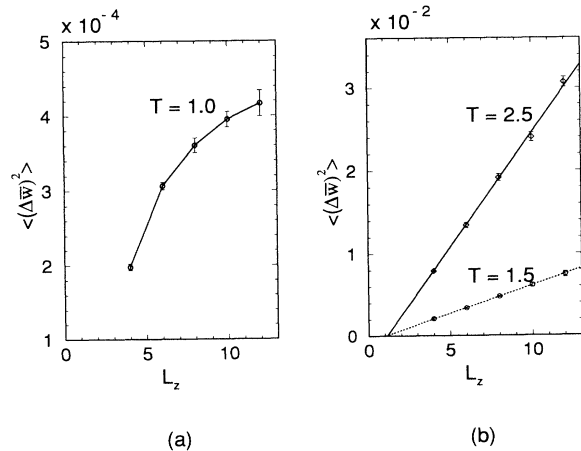


FIG. 5. Mean-square fluctuation, $\langle (\Delta \bar{\mathbf{w}})^2 \rangle$, of $\bar{\mathbf{w}}(z)$ is plotted vs stacking direction size L_z with locked phase (a) and unlocked phases (b).

and 2.5. The initial configuration within each layer is a sixth approximant. $\langle (\Delta \bar{\mathbf{w}})^2 \rangle$ does not show a linear dependence on L_z at $T = 1.0$, while it is linear in L_z at $T = 1.5$ and 2.5 (consistent with the earlier conclusion of an unlocked phase at $T = 1.5$ and 2.5). From the slope in Fig. 5(b) and Eq. (19), we find $cK_2 = 1.10 \pm 0.06$ at $T = 1.5$ and $cK_2 = 0.27 \pm .03$ at $T = 2.5$. Comparing these values to the elastic constants from the measurements of $\langle |\mathbf{w}(\mathbf{p})|^2 \rangle$, implies cutoff constant $c \sim 2$ in Eq. (19), while we have $a \simeq 1$ from Fig. 5.

B. Lane widths

As a mean of analyzing the low- T phase, we have measured the spacing between two adjacent trails in a layer.

A “trail” in our model is a contiguous strip of tiles, which share a common side-face direction (the side-face direction \mathbf{q}_α of a side face parallel to the plane spanned by $\mathbf{e}_\alpha^\parallel$ and \mathbf{e}_5^\parallel is $\mathbf{q}_\alpha = \mathbf{e}_\alpha^\parallel \times \mathbf{e}_5^\parallel$, $\alpha = 0, \dots, 4$). We shall call a trail, which has a side-face direction \mathbf{q}_α , an α -direction trail. An α -direction trail runs along the \mathbf{q}_α direction on average. As shown in Fig. 6, each layer consists of sets of parallel trails (Fig. 6 shows a layer in a fifth approximant system viewed from the tenfold axis). The regions between the trails will be referred to as “lanes.” In a perfect Penrose tiling, two different widths of lanes exist: a thick lane and a thin lane. These lanes repeat quasiperiodically (Fibonacci sequence) in the direction normal to the trail direction. Hence, in a locked phase, where this quasiperiodicity is believed not to be destroyed, the distribution of the lane widths is bimodal. The distribution under the one mode (corresponding thick lanes) is τ times bigger than that under the other mode, where τ is golden mean. In the unlocked phase, the distribution of the lane widths may have merged into one peak (as the distribution of the distances between nearest balls in a unlocked phase of Frenkel-Kontorova model³). With this in mind, we have measured the number of lanes $N^{\text{lane}} P(W) dW$ whose average width is in between W and $W + dW$,

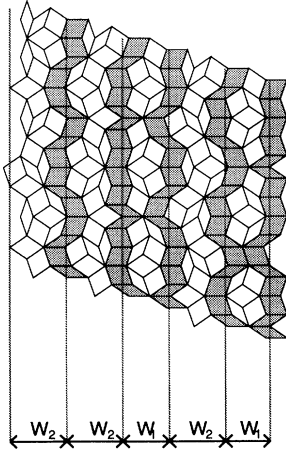


FIG. 6. Trails and lanes in a layer (above) and average widths of lanes (below). The sequences of the shaded tiles are trails. The region between neighboring trails is a lane. Average lane width is defined as the average of the spacing between two trails contiguous with that lane.

where N^{lane} is the total number of lanes in the system (average width of a lane is defined as the average of the spacing between two trails contiguous with the lane (see Fig. 6)). At low- T (at $T = 1.0$), as shown in Fig. 7(a), $P(W)$ has two peaks near the values corresponding the lane widths (W_1^{lock} and W_2^{lock}) of a Penrose tiling. As the system size diverges, lane widths converge the values of Penrose-tiling lane widths. In contrast, $P(W)$ at high- T [at $T=1.5$, Fig. 7(c)] shows a distribution with one peak at $W^{\text{unlock}} = L/N_{\alpha}^{\text{lane}}$ as $L \rightarrow \infty$, where L is the system size and N_{α}^{lane} is the number of α -direction lanes in a plane ($N_{\alpha}^{\text{lane}} = f_k$ for a k th approximant). $P(W)$ near the transition temperature (at $T = 1.3$) is shown in Fig. 7(b). From this figure, it is hard to tell whether the curve $P(W)$ at $T = 1.3$ will be bimodal (as in a locked phase) or be monomodal (as in a unlocked

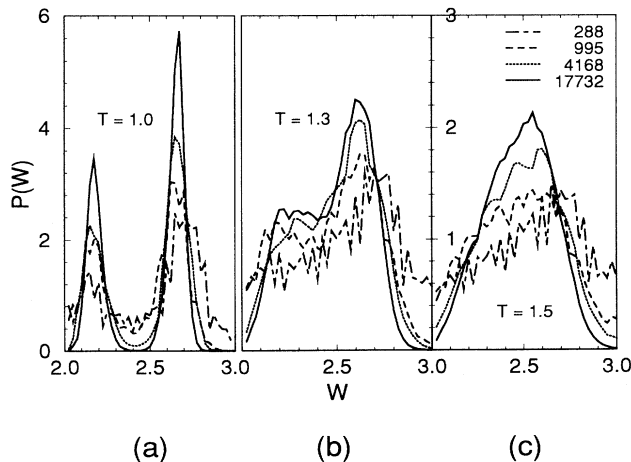


FIG. 7. Lane width distributions with locked phase (a) and unlocked phase (c). Lane width distributions near the transition temperature are shown in (b).

phase) as $L \rightarrow \infty$. We have checked reversality by doing some cooling runs from above T_c . The distribution of the lane widths merged into one peak at high T , come back to original bimodal mode with peaks at Penrose-tiling lane widths. This measurement of the distributions of the lane widths, suggests that the system is in locked phase at low temperature.

To estimate the transition temperature T_c we have measured the number of lanes whose widths are around the lane widths of a Penrose tiling and lanes with widths near W^{unlock} . Let us define P^{lock} and P^{unlock} as the relative number of these lanes:

$$\begin{aligned} P^{\text{lock}} &\equiv \int_{R_1} P(W)dW + \int_{R_2} P(W)dW, \\ P^{\text{unlock}} &\equiv \int_{R_3} P(W)dW, \\ P &\equiv P^{\text{lock}} - P^{\text{unlock}}, \end{aligned} \quad (20)$$

where $R_1 \equiv (W_1^{\text{lock}} - \delta_1, W_1^{\text{lock}} + \delta_1)$, $R_2 \equiv (W_2^{\text{lock}} - \delta_1, W_2^{\text{lock}} + \delta_1)$, and $R_3 \equiv (W^{\text{unlock}} - \delta_2, W^{\text{unlock}} + \delta_2)$. Here, δ_1 and δ_2 are small numbers ($\ll 1$) with $\delta_2 = 2\delta_1$. Then P should be 1 at $T = 0$ and should be negative at $T = \infty$ (the precise value at $T = \infty$ depends on the choice of δ_1 and δ_2 but greater than -1 always).

Figure 8 shows P vs temperature for a sequence of lattices of increasing size. We have chosen $\delta_1 = 0.05$ and $\delta_2 = 0.1$. P converges to 1 at low T and has negative values at high T . We roughly estimate the transition temperature $T_c \sim 1.3$ from Fig. 8 as the value around which the graphs of different sizes cross each other.

C. Trail magnetization

As a new order parameter to analyze the low- T phase and the transition from the low- T phase, we have devised a novel measure that we have termed trail magnetization. Trail-magnetization traces the ordering of “hexag-

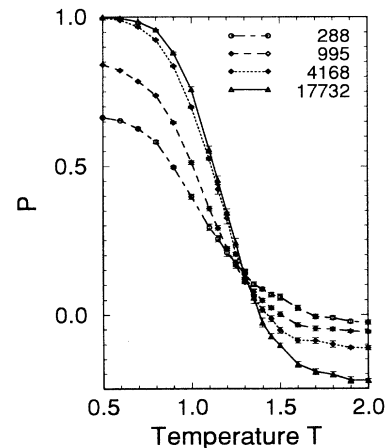


FIG. 8. System size dependence of P defined in Eq. (20) vs temperature.

onal prisms" along worms and trails that run through each layer.

A hexagonal prism, as shown in Fig. 2, consists of three tiles. The type (D or Q) of a hexagonal prism is identified with the type of the center vertex on the upper hexagon of the hexagonal prism.¹¹ By convention, the orientation of a hexagonal prism is "+" ("−") if the center vertex has an edge leading away from it along direction $\mathbf{e}_\alpha^\parallel$ ($-\mathbf{e}_\alpha^\parallel$). A worm in a layer is an unbroken sequence of hexagonal prisms and the length of a worm is defined to be the number of consecutive, connected hexagonal prisms. Flipping one hexagonal prism in a perfect worm creates a mismatch along either side face adjoining the worm (flipping the hexagonal prism again annihilates the mismatches). If we restrict flipping to only one worm, the 2D Penrose model is analogous to the one-dimensional Ising model, assigning "spin up" for one orientation hexagon and "spin down" for the flipped hexagon in a worm. If the 2D Penrose tiling were an aggregation of uncoupled worms (i.e., uncoupled one-dimensional Ising models), we would expect an order-disorder transition at $T = 0$, which coincides with the result that the transition to the unlocked phase in 2D Penrose tiling is at $T = 0$.

Along a trail, many worms (chains of hexagonal prisms) may be found. Along any trail in a perfect Penrose tiling, all worms longer than one hexagonal prism have the same orientation. Different trails may have opposite hexagonal prism orientation. Also, some worms of length one point in the opposite direction to the other hexagons in a trail. All together, about 97% of hexagonal prisms in a trail have same orientation in a perfect Penrose tiling, while the hexagonal prisms along a trail in a maximally random tiling have orientations which average to zero.¹⁷ Hence, we define the trail magnetization in α orientation

$$m_\alpha^{\text{tr}} = \frac{1}{N_\alpha^{\text{hexa}}} \sum_{i \in \{\text{tr}_\alpha\}} \left| \sum_{j \in \text{tr}_\alpha^i} S_j \right|, \quad (21)$$

where N_α^{hexa} is number of hexagons in α -direction trails,

$\{\text{tr}_\alpha\}$ means all trails ($f_k \times L_z$ trails for a k th approximant) in the α -direction, and tr_α^i means the i th trail in α direction ($i = 1, \dots, f_k \times L_z$). Here, spin variable S_j is assigned to the j th hexagonal prism and takes ± 1 depending on the orientation of the hexagonal prism. Without loss of generality, we will discuss results for $\alpha = 0$ (\mathbf{e}_0^\parallel -direction trails).

Figure 9 shows the trail magnetization and "trail susceptibility"

$$\chi_m = N_{\text{hexa}} \frac{1}{T} (\langle (m^{\text{tr}})^2 \rangle - \langle m^{\text{tr}} \rangle^2), \quad (22)$$

and illustrates how m^{tr} can serve as a useful diagnostic measure. At $T = 0$, the trail magnetization converges to a fixed value as the system diverges, a value consistent with the expectation value for a locked, Penrose-tiling phase. At $T \geq 1.5$, the trail magnetization approaches zero as $L \rightarrow \infty$, consistent with an unlocked phase. The magnitude of susceptibility maximum seems to diverge near the transition temperature. To obtain the transition temperature and critical exponents, we attempt to fit the trail magnetization and susceptibility according to

$$m^{\text{tr}}(T, L) = L^{-\beta/\nu} f[(T - T_c)L^{1/\nu}], \quad (23)$$

$$\chi_m(T, L) = L^{\gamma/\nu} g[(T - T_c)L^{1/\nu}], \quad (24)$$

where L is the system size, T_c is transition temperature of the infinite system and critical exponents β , γ , ν are defined from the temperature dependence of order parameter m^{tr} , susceptibility χ_m , and the correlation length ξ near the transition temperature:

$$\begin{aligned} m^{\text{tr}} &\sim (T - T_c)^\beta \quad \text{for } (T < T_c), \\ \chi_m &\sim |T - T_c|^{-\gamma}, \\ \xi &\sim |T - T_c|^{-\nu}. \end{aligned}$$

In Fig. 10(a), we plot $m^{\text{tr}}(T, L) L^{\beta/\nu}$ vs $(T - T_c)L^{1/\nu}$ and in Fig. 10(b), $\chi_m(T, L) L^{-\gamma/\nu}$ vs $(T - T_c)L^{1/\nu}$, for values

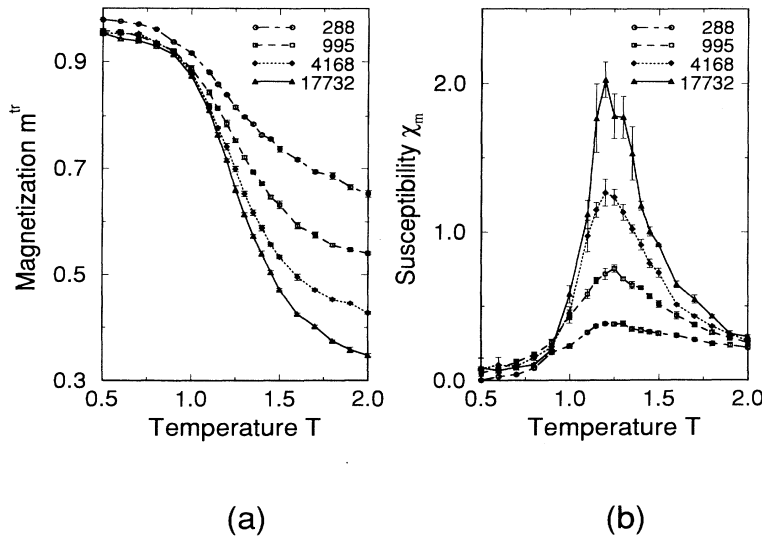
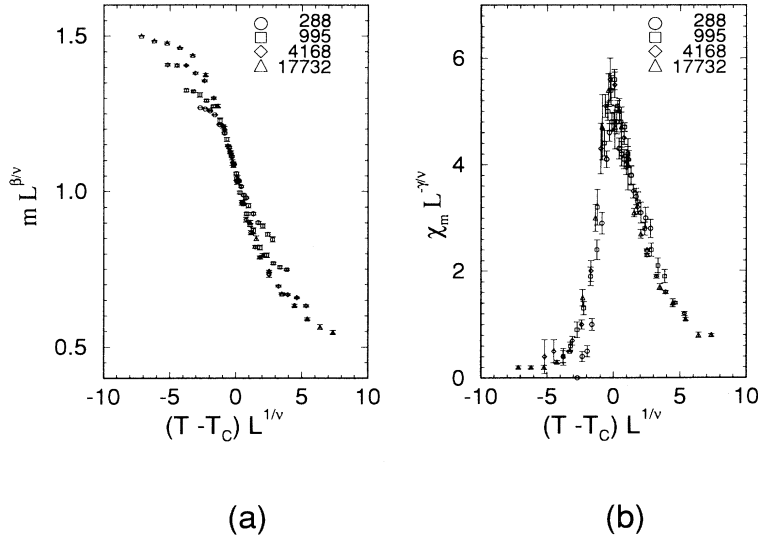


FIG. 9. System size dependence of the trail magnetization (a) and susceptibility (b) plotted against temperature.



$$T_c = 1.24, \quad \beta = 0.2, \\ \gamma = 1.6, \quad \nu = 1.6.$$

The m^{tr} and χ_m curves for various system size superimpose clearly. We have checked the possibility of a sequence of transitions rather than a single transition by considering

$$m'^{\text{tr}}_\alpha = \frac{1}{N_\alpha^{\text{hexa}}} \sum_{i \in \{\text{tr}_\alpha\}} \left| \sum_{j_i \in \text{tr}_\alpha^i} S_{j_i} \right|, \quad (25)$$

where tr_α^i traces over the i th trails in all layers along direction α . (To see the ordering in stacking direction also, we took a sum of spin variables in i th trails of all L_z layers before taking the absolute values instead of summing the spin values in each individual trail as in m^{tr} .) We have been able to make m'^{tr} and $\chi_{m'}$ curves for various system size superimpose. The transition temperature from the measurement of m'^{tr} is consistent with the result from m^{tr} .

We also measured energy per tile $\langle \varepsilon \rangle = \langle E/N \rangle$ and specific heat $C_v = (\frac{1}{T})^2 (\langle \varepsilon^2 \rangle - \langle \varepsilon \rangle^2) N$, where E is the system energy given by Eq. (1) and N is number of tiles. Specific heat has its maximum near the transition temperature T_c and the magnitude of its maximum seems to be independent of the system size (Fig. 11) implying that the specific-heat exponent $\alpha = 0$, where α is defined by

$$C_v \sim |T - T_c|^{-\alpha}.$$

The results of trail magnetization and specific-heat measurements seem very consistent with a single continuous transition from a locked phase ($m^{\text{tr}} \approx 1$) to an unlocked phase.

To check the robustness of the result, we have repeated the analysis for other related models. First we changed the interaction strength ratio $\varepsilon_1/\varepsilon_2$. Recall that the net energy cost of a hexagonal prism flip is $2\varepsilon_1 + 6\varepsilon_2$. We have tested $\varepsilon_1/\varepsilon_2 = 1$ and $\varepsilon_1/\varepsilon_2 = 9$ and found that the

FIG. 10. Finite-size scaling plots of the data for trail magnetization, shown in Fig. 9(a), and for susceptibility, shown in Fig. 9(b). Here, $mL^{\beta/\nu}$ (a) and $\chi_m L^{-\gamma/\nu}$ (b) are plotted versus $(T - T_c)L^{1/\nu}$ with the following choice of exponents: $\beta = 0.2$, $\gamma = 1.6$, and $\nu = 1.6$ and the transition temperature $T_c = 1.24$.

systems show a locked-phonon to unlocked-phonon phase transition at finite temperature.

We have also considered models, where we have relaxed the interlayer “stacking constraint” (that a hexagonal prism can be flipped only if a hexagonal prism lies just above or below with sharing a same hexagon boundary in between; see Sec. II). The low-temperature phase of this model appears to be the same as that of the model with the stacking constraint. At high temperature ($T > T_c$), free energy shows a quadratic dependence on spatial variation in phason variable in a layer ($|\partial_x \mathbf{w}|^2 + |\partial_y \mathbf{w}|^2$). For the stacking direction, free energy shows a quadratic behavior in $(\partial_z \mathbf{w})$ up to some temperature T'_c ($T'_c > T_c$), which depends on the system size. Above the T'_c , layers become decoupled so that the averaged phason field $\bar{\mathbf{w}}(z)$ of z th layer [Eq. (16)] is not correlated with $\bar{\mathbf{w}}(z \pm 1)$ [correlation length of $\bar{\mathbf{w}}(z)$ is zero for $T > T'_c$]. However, T'_c increases as the system size is getting bigger and we speculate that T'_c may diverge in the thermodynamic limits.

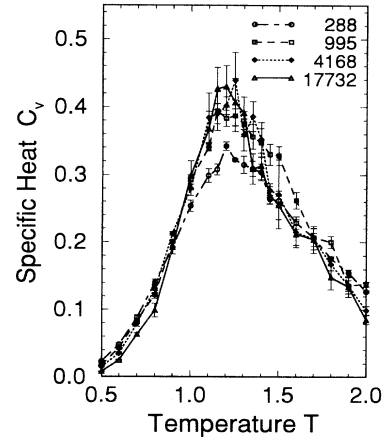


FIG. 11. System size dependence of specific heat plotted against temperature.

V. CONCLUSIONS

Our paper presents systems that show a finite-temperature locked-phason-to-unlocked-phason phase transition in quasicrystals. All models for 3D decagonal quasicrystals we have studied show a single continuous phase transition at finite temperature from low- T locked phase to high- T unlocked phase.

Phason fluctuations of the system show strong evidences that the system is in unlocked phase at $T > T_c$ in which free energy is described as square gradient of phason variables. At $T < T_c$, from the measurements of lane width and trail magnetization, we conclude that the system is in locked phase. The finite specific-heat peak and the critical exponents we obtained from the scaling behaviors of the m^{tr} show that the transition is continuous.

Recently Hiraga *et al.* have noted that the periodically spaced layers in ALPbMn decagonal quasicrystals strongly correlated atomic order. Our simulations show that there is a single transition in which both intralayer and interlayer phason fluctuations transform from locked to unlocked. Hence, the observation of correlated order (locking) between layers would imply that that ALPbMn quasicrystals are in the locked phase and not in the random tiling in spite of some apparent disorder within the layer. (The disorder is likely to be due to decapod defects or unusual local isomorphism class.)

To predict the transition temperature T_c in real quasicrystals, we need to know how big the mismatch energies (ϵ_1 and ϵ_2) are. Note that T_c is of order the geometric mean mismatch energy $\epsilon = (\epsilon_1\epsilon_2)^{\frac{1}{2}}$ for our model. T_c will

approach zero if either ϵ_1 or ϵ_2 approaches zero.

The unlocking transition could be preempted by the melting transition. If the transition temperature T_c is higher than the melting temperature T_m , quasicrystals remain in the locked phase for temperatures ranging all the way up to melting point. For these systems, one would expect more quenched phasons than for a system, which has unlocked phase between the melt phase and the locked phase, since unlocking implies rapid relaxation of phason fluctuations. Hence, the relation between T_c and T_m may partially account for the reason why some systems form near-perfect quasicrystals and others do not. For the system that has an unlocked phase ($T_c < T_m$), the transition from the unlocked phase to the locked phase could be observed in experiments. An observational effect could be Debye-Waller suppression of the diffraction peak intensities. In the unlocked phase, phasons can be thermodynamically excited. As we can see in Fig. 3, the phason elastic constants increase with decreasing temperature in the unlocked phase. Consequently, the Debye-Waller suppression decreases as T decreases toward T_c . Then, after the transition to the locked phase, thermal phason fluctuations are frozen and the the Debye-Waller suppression disappears.

ACKNOWLEDGMENTS

We would like to thank Tomonari Dotera for many useful discussions. We also thank C. L. Henley and M. Widom for critical reading of the manuscript. This research was supported by the DOE at Penn (DOE-EY-76-C-02-3071).

- ¹ D. Levine, T. C. Lubensky, S. Ostlund, S. Ramaswamy, P. J. Steinhardt, and J. Toner, *Phys. Rev. Lett.* **54**, 1520 (1985).
- ² L. Bendersky, *Phys. Rev. Lett.* **55**, 1461 (1985).
- ³ For a review, see P. Bak, *Rep. Prog. Phys.* **45**, 587 (1982).
- ⁴ D. Levine and P. J. Steinhardt, *Phys. Rev. Lett.* **53**, 2477 (1984).
- ⁵ A. R. Kortan, F. A. Thiel, H. S. Chen, A. P. Tsai, A. Inoue, and T. Masunoto, *Phys. Rev. B* **40**, 9397 (1989).
- ⁶ P. J. Steinhardt and D. P. DiVincenzo, in *Quasicrystals: The World of the Art*, edited by D. P. DiVincenzo and P. J. Steinhardt (World Scientific, Singapore, 1991).
- ⁷ C. L. Henley, in *Quasicrystals: The State of the Art* (Ref. 6).
- ⁸ J. E. Socolar, T. C. Lubensky, and P. J. Steinhardt, *Phys. Rev. B* **34**, 3345 (1986).
- ⁹ P. A. Kalugin, *Pis'ma Zh. Eksp. Fiz.* **49**, 406 (1989) [*JETP Lett.* **49**, 406 (1989)].
- ¹⁰ L.-H. Tang and M. V. Jaric, *Phys. Rev. B* **41**, 4524 (1990).

- ¹¹ N. G. de Bruijn, *Nederl. Akad. Wetensch. Proc. Ser. A* **84**, 39 (1981).
- ¹² M. C. Shin and C. Strandburg, *Non-Crystal. Sol.* **153&154**, 253 (1993).
- ¹³ Those who are not familiar with Monte Carlo simulation terminology, see, for example, K. Binder and D. W. Heermann, *Monte Carlo Simulation in Statistical Physics* (Springer-Verlag, Berlin, 1988).
- ¹⁴ L. J. Shaw, V. Elser, and C. L. Henley, *Phys. Rev. B* **43**, 3423 (1991).
- ¹⁵ M. Oxborrow and C. L. Henley, *Phys. Rev. B* (to be published).
- ¹⁶ A. M. Ferrenberg and R. H. Swendsen, *Phys. Rev. Lett.* **63**, 1195 (1989).
- ¹⁷ For the maximally random tiling, the orientations are correlated but sufficiently weak that the average approaches zero in the limit of infinite trail length.
- ¹⁸ K. Hiraga and W. Sun (unpublished).